Supplementary Information

Deciphering the Interplay between Tin Vacancies and Free Carriers in the Ion Transport of Tin-Based Perovskites

*Luis Huerta Hernandez, Luis Lanzetta, Anna M. Kotowska, Ilhan Yavuz, Nikhil Kalasariya, Badri Vishal, Marti Gibert-Roca, Matthew Piggott, David J. Scurr, Stefaan De Wolf, Martin Stolterfoht, Derya Baran**

Luis Huerta Hernandez, Luis Lanzetta, Badri Vishal, Marti Gibert-Roca, Stefaan De Wolf, & Derya Baran

Materials Science and Engineering Program (MSE), Physical Sciences and Engineering Division (PSE), King Abdullah University of Science and Technology (KAUST), Thuwal 23955-6900, Saudi Arabia

e-mail: derya.baran@kaust.edu.sa

Anna M. Kotowska, Matthew Piggott, & David J. Scurr

Advanced Materials and Healthcare Technologies, School of Pharmacy, University of Nottingham NG7 2RD, United Kingdom

Ilhan Yavuz

Marmara University, Physics Department, 34722, Kadikoy, Istanbul, Turkiye

Nikhil Kalasariya & Martin Stolterfoht

Electronic Engineering Department, The Chinese University of Hong Kong, Sha Tin N.T., Hong Kong SAR, China

Supplementary Notes

Supplementary Note 1: There are several important assumptions that are considered for the galvanostatic polarization measurements performed in this work. Herein, we provide a brief discussion on these:

1. The accumulation of ions at the interfaces with contacts can influence the energy barriers for carrier extraction/injection. Errors in the estimation of the ionic and electronic conductivities may arise depending on how the energy barriers are influenced by the ions. However, since we are measuring devices with symmetrical contacts under relatively low bias (where ohmic behavior is observed) and dark conditions (where no recombination occurs), we expect this phenomenon to have minor implications on the calculations of ionic and electronic conductivities.

2. Another important assumption is that electrodes are unreactive with the perovskite. In the majority of galvanostatic polarization studies on metal halide perovskites, Au is the common choice as the electrode.[1-3] To test this assumption, we conducted repeated galvanostatic polarization measurements on samples with silver (Ag/$FASn_{0.5}Pb_{0.5}I_3$/Ag) and gold (Au/$FASn_{0.5}Pb_{0.5}I_3$/Au) electrodes (Figure S1). For both electrode configurations, we note significant alterations in the total conductivity with each measurement cycle. Interestingly, during the 1st measurement cycle of the Au sample, we recorded an increase in voltage during the initial 100 s, followed by a continuous voltage decrease. In the subsequent cycles, we only recorded a drop in voltage, signaling an increase in the total conductivity during the measurement. In contrast, repeated measurements on Cr/Au contacts (Au/Cr/$FASn_{0.5}Pb_{0.5}I_3$/Cr/Au) reveal a significantly more stable behavior.

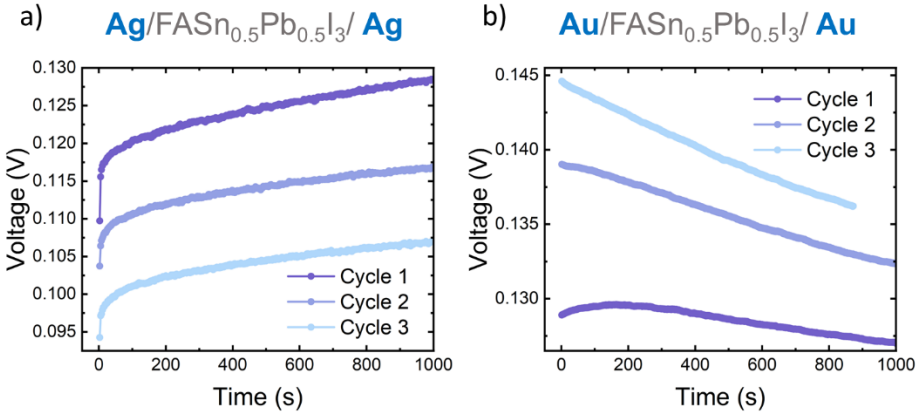

Figure S1. a) Galvanostatic polarization curves of Ag/$FASn_{0.5}Pb_{0.5}I_3$/Ag and b) Au/$FASn_{0.5}Pb_{0.5}I_3$/Au. A rest period of 90 minutes was implemented between each measurement to allow the mobile ions to return to their initial state.

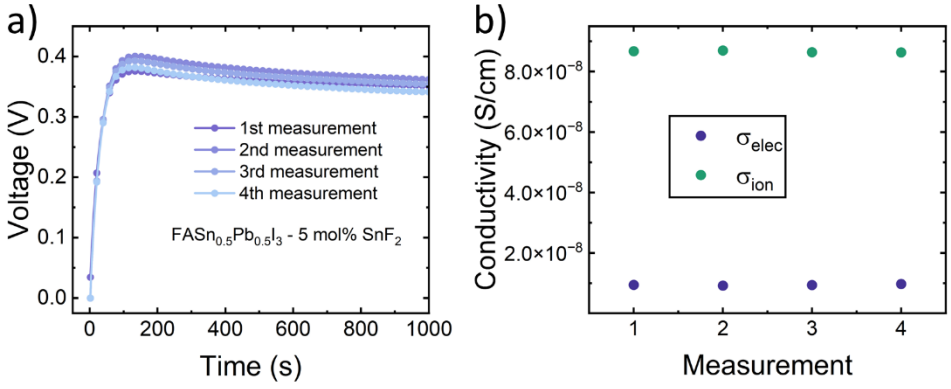

Figure S2. a) Multiple galvanostatic polarization curves from Au/Cr/$FASn_{0.5}Pb_{0.5}I_3$/Cr/Au sample . b) Extracted σ_{elec} and σ_{ion} from each measurement cycle (right panel). A rest period of 90 minutes was implemented between each measurement to allow the mobile ions to return to their initial state.

To investigate more about the instability and the voltage transients of Au/$FASn_{0.5}Pb_{0.5}I_3$/Au samples, we analyzed the samples after performing the three measurement cycles with SEM imaging (Figure S3). The micrographs revealed a substantial accumulation of white particles at the positive electrode and extending into the channel. Similar formation of such particles has been documented in perovskite field effect transistors following continuous biasing cycles, where the authors suggested that these white particles consist of gold.[4] In contrast, we detected a considerable reduction of these particles in the Au/Cr samples, suggesting that Cr slows down the Au migration.[4-6] Considering the known reactivity of Ag and Au with the perovskite and their low diffusion barriers it is plausible that the changes in conductivity in these systems are strongly influenced by interfacial reactions and metal diffusion.[7-10] Hence, we concluded that the Au/Cr/Perovskite/Cr/Au is a more stable and reliable architecture to perform the galvanostatic polarization measurements.

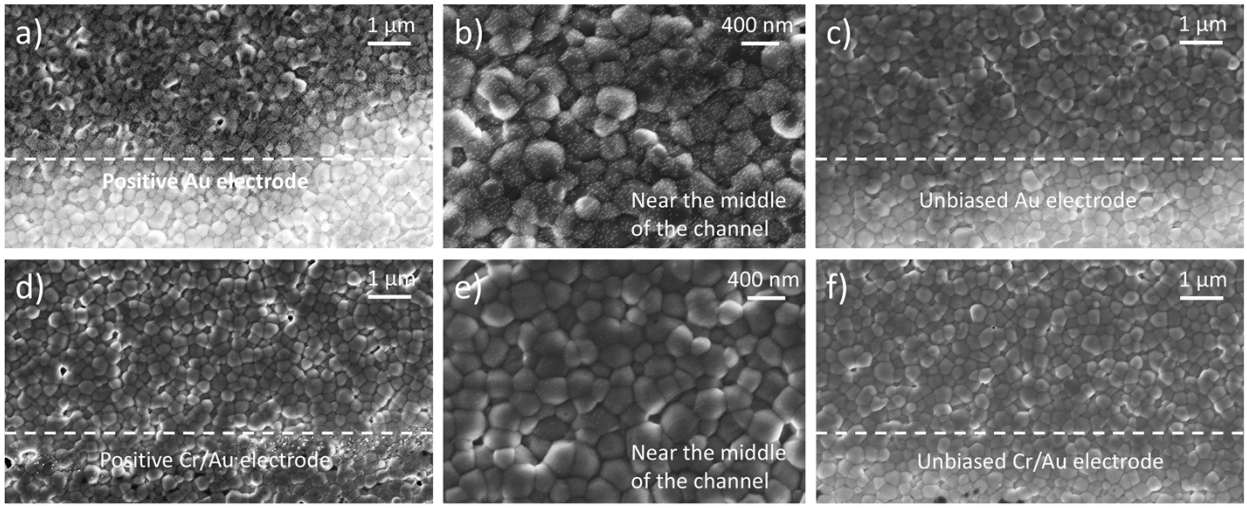

Figure S3. SEM images of the region near the positive electrode of a) Au/$FASn_{0.5}Pb_{0.5}I_3$/Au and d) Au/Cr/$FASn_{0.5}Pb_{0.5}I_3$/Cr/Au samples after three galvanostatic polarization measurement cycles, b) near the middle of the channel, and c) an unbiased sample as reference.

3. The formation of more mobile ionic species caused by the measurement conditions is another possibility where overestimation of ionic conductivity could be observed. As shown in Pb perovskites, holes can oxidize iodide species resulting in the generation of iodide interstitials that may contribute to higher ionic conductivity.[11, 12] In the case of Sn-based perovskites, oxidation of iodide has been suggested to be energetically less unfavorable due to shallower valence band energy levels.[13] In Figure S1, we performed a galvanostatic polarization measurement for 5000 s. We observe that voltage changes from 1000 s to 5000 s are minimal compared to the changes occurred during the initial 1000 s. This is better represented by the normalized derivative of the voltage relative to time, this quantity indicates how large are the voltage changes with time. From this value, we can clearly observe that 99.9% of the voltage changes happened during the first 1000 s of measurement. The remaining 0.01% could be explained in terms of: i) slower-moving ionic species ii) creation of new mobile ions during measurement conditions and iii) electrochemical reactions at the perovskite/electrode interface that modify charge extraction barriers. To minimize

perovskite or perovskite/interface damage, we measured under low voltages (in the ≈10^{-1} V region) and under relatively short periods of time (≤1000 s).

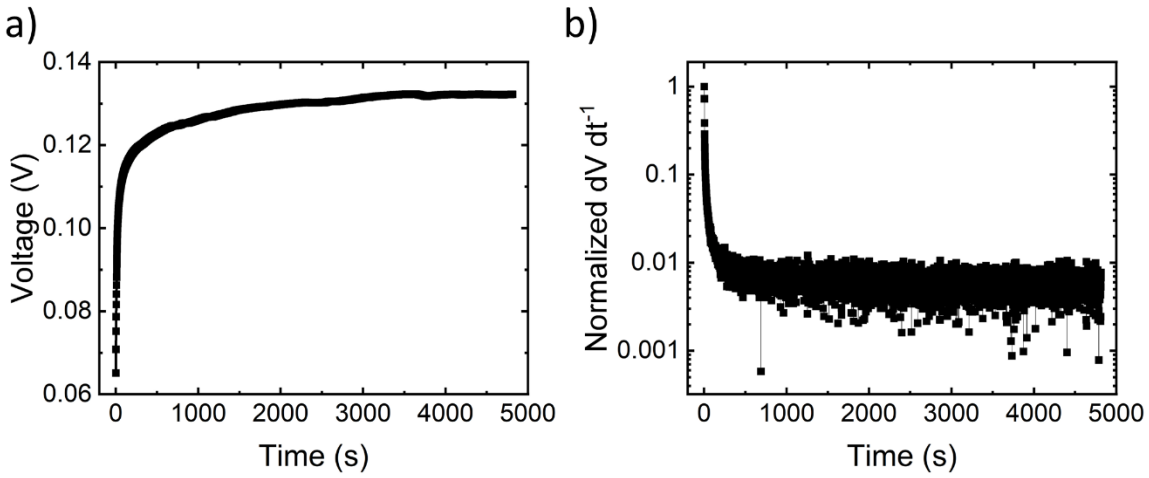

Figure S4. a) Galvanostatic polarization curve of Au/Cr/$FASn_{0.5}Pb_{0.5}I_3$/Cr/Au sample taken during 5000 s and b) the normalized derivative of the voltage relative to time.

Supplementary Note 2: The reduced bandgap of the Sn-containing perovskites may contribute to the enhancement in $[p]$. However, we do not consider the bandgap narrowing as the dominant factor behind the higher σ_{elec}, as $ASn_{0.5}Pb_{0.5}I_3$ samples possess a narrower bandgap (1.2-1.3 eV) but orders of magnitude lower σ_{elec} than only Sn compositions (1.3-1.4 eV).[14]

Supplementary Note 3: Past research has demonstrated that SnF_2 regulates the concentration of V_{Sn}^{2-}, and hence the hole carrier concentration, via two mechanisms. The first is by capturing the Sn^{4+} impurities that might be already in the precursor materials (i.e. as SnI_4) or that could arise during film fabrication.[15] F^- ions coordinate preferentially with Sn^{4+}, inducing a ligand exchange reaction as follows:

$$SnI_4 + 2SnF_2 \rightarrow SnF_4 + 2SnI_2$$

The formation of SnF_4 prevents the incorporation of Sn^{4+} in the perovskite lattice, resulting in a reduction of V_{Sn}^{2-}.

The alternative mechanism on how SnF_2 controls the V_{Sn}^{2-} is related to an increase in the chemical potential of the Sn^{2+} ions. DFT calculations have demonstrated that growing a $MASnI_3$ perovskite under Sn-rich conditions, results in an increase in the formation energy of V_{Sn}^{2-} compared to stoichiometric growth conditions, which leads to a reduction in the p-doping.[16] The Sn-rich conditions can be experimentally achieved with any of the Sn^{2+} halides, including Cl^-, Br^-, or I^-,[15] which explains why other Sn^{2+} halides similarly reduce the hole density.[17] Given the broad relevance of SnF_2 in the state-of-the-art Sn-based perovskite photovoltaics, we decided to focus on this additive to tune the V_{Sn}^{2-} and $[p]$.

Supplementary Note 4: The chemical diffusion coefficient (D^{δ}) can provide an approximate estimation of μ_{ion}. The D^{δ} is determined by the contribution of the ionic and electronic diffusion coefficients (D_{ion} and D_{elec}, respectively):[3]

$$D^{\delta} = \frac{\sigma_{elec}}{\sigma_{elec} + \sigma_{ion}} D_{ion} \mathrm{X}_{ion} + \frac{\sigma_{ion}}{\sigma_{elec} + \sigma_{ion}} D_{elec} \mathrm{X}_{elec}$$

where X_{ion} and X_{elec} are the ionic differential trapping factor and electronic differential trapping factor, respectively. D_{ion} and D_{elec} are proportional to the ionic and charge carrier mobility, respectively:[18]

$$D_{ion} = \mu_{ion} \frac{k_B T}{q}$$

$$D_{elec} = \mu_{elec} \frac{k_B T}{q}$$

where k_B is the Boltzman constant, T is the temperature, and q is the particle charge.

We estimated D^{δ} from the galvanostatic polarization curves found in Figure 2a. Using the following relation: $V = V(t = a) \cdot \left(1 - e^{-t/\tau}\right)$,[18] where V(t=a) is the steady-state voltage that is reached at $t = a$ (as shown in Figure 1a), t is the time, and τ is the time constant; τ is extracted from the slope of the linear relationship between $\ln\left(V(t = a) - V\right)$ and t (Figure S8). Then, D^{δ} can be inferred from:

$$D^{\delta} = \frac{d^2}{\pi^2 \tau}$$

where d is the sample thickness.

We noticed that increasing the SnF_2 concentration from 0 to 10 mol% reduced the D^{δ} from 5.56 x 10^{13} cm^2 s^{-1} to 1.82 x 10^{13} cm^2 s^{-1} (Figure S13). Considering that μ_h remains relatively constant with the addition of SnF_2, then the reduction of D^{δ} may be indication of a lower D_{ion} and consequently a lower μ_{ion}. However, the complex dependence of D^{δ} on both electronic and ionic components impedes to quantify the individual role of the μ_{ion} on the D^{δ}. A more specific analysis on the role of D^{δ} and μ_{ion} on mixed ion-electronic transport lies outside the scope of this work and will be shown in future work.

Supplementary Note 5: Since different ionic-electronic transport phenomena occurs at different timescales, the capacitance of perovskite devices strongly depends on the frequency of the voltage signal. Empirically, the capacitance vs frequency plot typically suggests two frequency regions of interest: i) Mid to high-frequencies (10^1-10^5 Hz): This region is characterized by a plateau in the capacitance, indicating that capacitance variations are minimal with respect to frequency. The geometrical capacitance and fast electronic processes such as trap-assisted recombination, carrier generation, and transport have shown to dominate the capacitance response in this region. ii) Low-frequency (10^{-1}-10^1): The distinctive feature in this region is a significant increase in the capacitance. While several theories have been proposed to explain this behavior, extensive drift-diffusion simulations combined with experimental data have demonstrated that mobile ion density governs the capacitance at lower frequencies.[19-22] Therefore, the capacitance as a function of voltage can provide information related to ionic or electronic processes depending on the frequency of the voltage signal.

Nevertheless, it remains difficult to completely disentangle the effect of traps and ions. Hence, we cannot fully rule out the effect of localized phonon vibrations, particularly those around the V_{Sn}^{2-}. Because of this, we have performed other two different measurement techniques to cross-check the trend we observe in the n_{ion} when changing the concentration of SnF_2. One of this is simply the capacitance as a function of frequency (Figure S14), where we noticed in the lower frequency regions an increase in capacitance with higher SnF_2 concentrations, suggesting a higher n_{ion}. Another technique utilized was bias assisted charge extraction (BACE), where instead of measuring capacitance changes, it tracks a transient ionic current caused by an external electric field (Figure 3d). Considering the consistent n_{ion} trend we detected across all these measurements and the results from the galvanostatic polarization technique, we are confident about the robust correlation between SnF_2 concentration and n_{ion} shown in our results.

Supplementary Note 6: During the measurement shown in Figure S17, we noticed that the PL intensity of the 0, 2.5, and 5 mol% samples did not change significantly for the duration of the measurement. However, the PL emission of the 10 mol% sample increased up to 6% after 10 min. We attribute this change to a light-induced charge trapping effect. This phenomenon commonly occurs in perovskites where photogenerated carriers can effectively fill trap states, leading to an increase in the PL emission.[23] Notably, this only occurs for samples with the highest content of SnF_2, which suggest a possible increase in the defect density. It has been previously reported that at high concentrations (>5 mol%) of SnF_2 in $Cs_{0.15}FA_{0.85}Sn_{0.5}Pb_{0.5}I_3$, results in an increase in defect density.[24]

Supplementary Note 7: We propose that the absence of I and Sn in the EDS elemental mappings (Figures 5c an S18a) can be explained by the excess of h^+ and V_I^+ expected at the cathode. As demonstrated by past reports, h^+ and V_I^+ favor the oxidation of I^- and Sn^{+2} into I_2 and SnI_4, respectively.[25-27] Considering the volatility of these products and that the measurements were carried under high vacuum, we suspect that the sublimation of both species took place inside the SEM chamber; hence, reducing the amount of I and Sn in the region near the electrode.

Supplementary Note 8: The permanent efficiency losses observed in the 0 mol% SnF_2 devices are most likely associated with an interfacial degradation. We hypothesize that the perovskite/PEDOT:PSS interface is where most changes would take place during forward bias, as a high accumulation of I^- is expected at this interface. Under such I^- rich conditions, we propose several phenomena that could explain the observed permanent performance loss:

- Iodide oxidation induced by excess hole carriers: In Pb perovskites, electrochemical hole injection has been shown to initiate the oxidation I^- into I_2 and I_3^-. While this remains to be observed in Sn-based perovskites, it could be a possibility considering the compositional inhomogeneity of the film.[11, 12] Our group has recently observed that Sn^{2+} oxidation through I_3^- is a rapid reaction that promotes further degradation pathways.[28] This suggest that a potentially degraded interface could be generated after biasing.
- Perovskite amorphization at the interface: Changes in the perovskite crystallinity triggered by an excess of I^- can lead to the formation of deep trap defects, enhancing non-radiative recombination.[29]

- Changes in the conductivity of PEDOT:PSS caused by the diffusion of iodides: Disruption of the structural homogeneity of PEDOT:PSS by iodides might result in the formation of trap states or impaired hole collection efficiency.[30]

Finally, we highlight that it is not within the scope of this work to explain in full detail the process of bias-induced degradation, but to show the mechanism behind the mixed-ionic electronic transport in Sn-based perovskites. However, we do establish that significant bias-induced efficiency losses in SnPb perovskites are linked to the ion transport properties of these materials. Further work on the bias-induced degradation is currently under development and will be reported in due course.

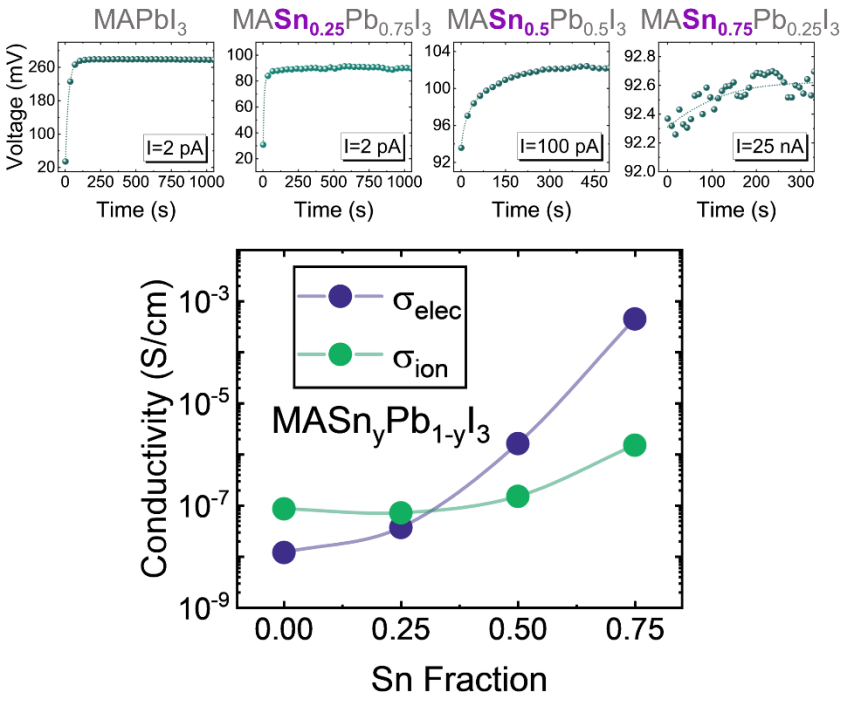

Fig. S5 Galvanostatic polarization curves from $MASn_yPb_{1-y}I_3$ (y=0, 0.25, 0.5, 0.75 and 1) samples.

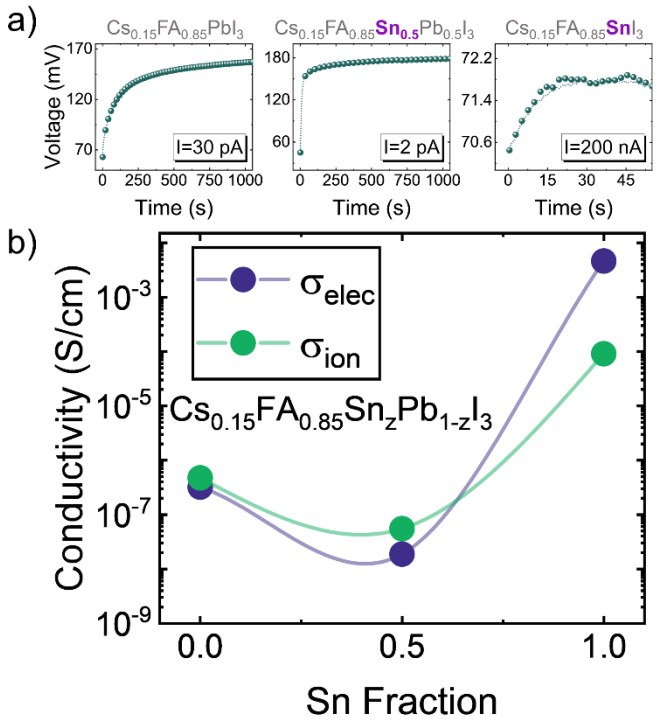

Fig. S6 a) Galvanostatic polarization curves from the compositions $Cs_{0.15}FA_{0.85}Sn_zPb_{1-z}I_3$ (z=0.0, 0.50, and 1.0) b) σ_{elec} and σ_{ion} from the $Cs_{0.15}FA_{0.85}Sn_zPb_{1-z}I_3$ samples as a function of Sn fraction. For this composition, we notice that substitution of 50% Sn leads to a decrease in σ_{elec} and σ_{ion}. This phenomenon could be explained due to an PbI_2 excess found in XRD measurements from the z=0 sample, such excess is not detected for the z=0.5 composition. The PbI_2 excess appears even if we used stoichiometric

conditions for sample preparation, possibly implying that i) annealing conditions need to be optimized, or ii) crystalline phase instabilities. Interestingly, the PbI_2 excess could potentially act as a n-type dopant increasing the σ_{elec}, while the σ_{ion} could be enhanced due to a more defective film. Notably, we observe a similar situation for the $FAPbI_3$ sample without MACl. In these compositions where structural phase instability is present, substitution of smaller Sn^{2+} ion relaxes the lattice structure, enhancing phase stability (under inert conditions) and possibly decreasing defect density.

MA Series			
Sn fraction	σ_{elec} **(S cm^{-1})**	**σ_{ion} (S cm^{-1})**	**t_{ion}**
0	1.20E-08	8.58E-08	0.88
0.25	3.69E-08	7.17E-08	0.66
0.5	1.63E-06	1.51E-07	0.08
0.75	4.50E-04	1.51E-06	0.01
1	NA	NA	NA
FA Series			
0	2.07E-08	1.64E-07	0.89
0.25	1.31E-08	7.87E-08	0.86
0.5	1.59E-08	7.96E-08	0.83
0.75	9.12E-06	8.28E-07	0.08
1	3.73E-04	3.50E-05	0.09
CsFA Series			
0	3.19E-07	4.75E-07	0.60
0.5	1.87E-08	5.51E-08	0.75
1	4.64E-03	9.11E-05	0.02

Table S1. Summary of the σ_{elec}, σ_{ion}, and t_{ion} from all the compositions measured. The ion transport number (t_{ion}) represents the ratio of ionic to total conductivity $\left(t_{ion} = \frac{\sigma_{ion}}{\sigma_{tot}}\right)$.

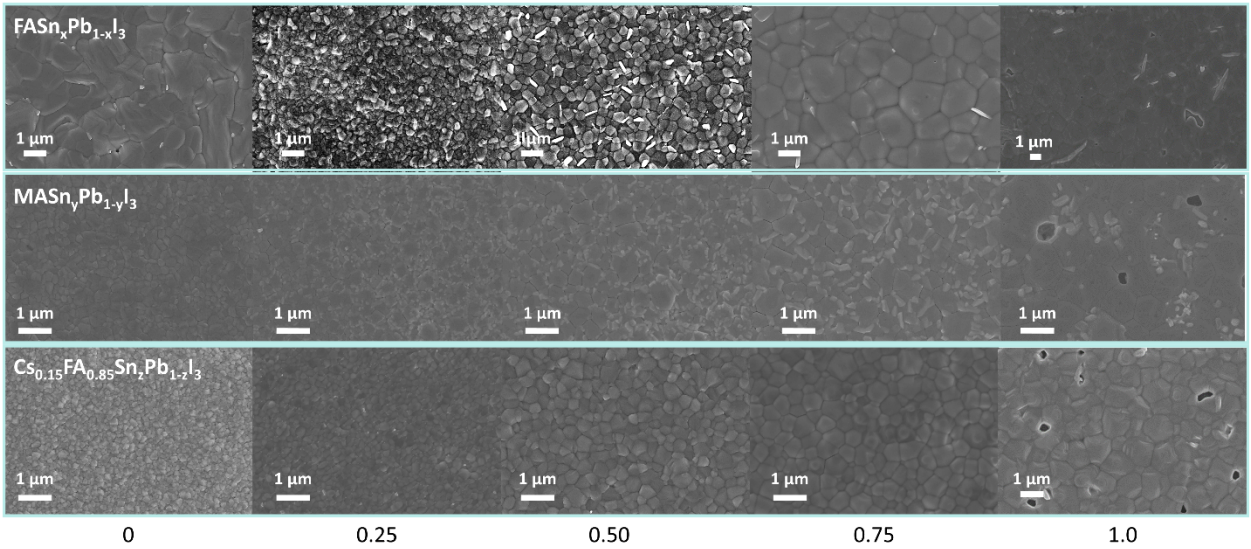

Fig. S7 SEM images from the $FASn_xPb_{1-x}I_3$, $MASn_yPb_{1-y}I_3$, and $Cs_{0.15}FA_{0.85}Sn_zPb_{1-z}I_3$ compositions.

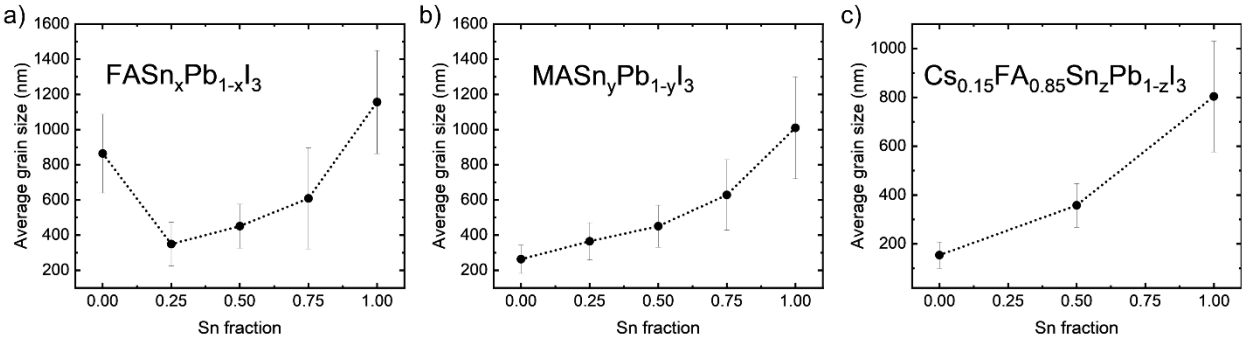

Fig. S8 Average grain size with respect to the Sn fraction from the compositions a) $FASn_xPb_{1-x}I_3$, b) $MASn_yPb_{1-y}I_3$, and c) $Cs_{0.15}FA_{0.85}Sn_zPb_{1-z}I_3$. The grain sizes were derived from the SEM images of Figure S3. Notably, the larger grain sizes observed in $FAPbI_3$ are a result of the MACl inclusion during the preparation of the precursor solution. Without this additive, we could not obtain a pure α-phase $FAPbI_3$. According to several reports, the majority of MACl is evaporated during the annealing step.[31] Hence, we expect that Cl^- or MA^+ ions do not have a substantial contribution in the ionic conductivity measurements.

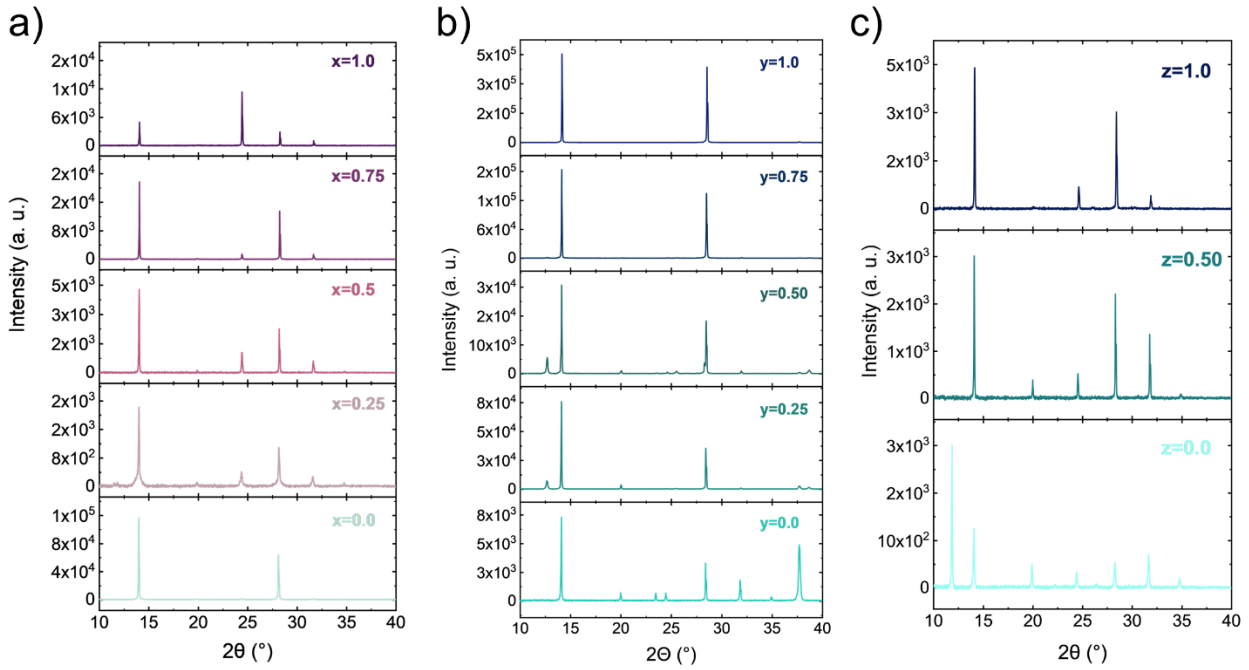

Fig. S9 XRD patterns of a) $FASn_xPb_{1-x}I_3$, b) $MASn_yPb_{1-y}I_3$, and c) $Cs_{0.15}FA_{0.85}Sn_zPb_{1-z}I_3$.

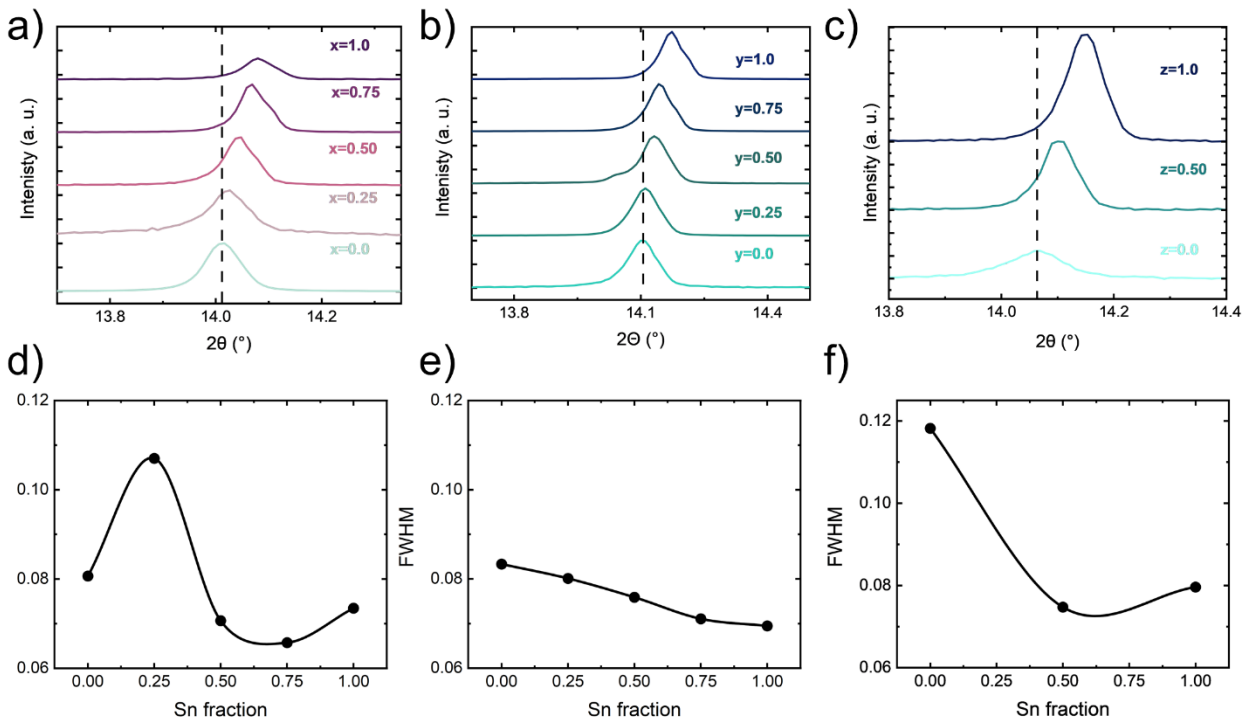

Fig. S10 XRD patterns of the characteristic perovskite peak from a) $MASn_xPb_{1-x}I_3$, b) $FASn_yPb_{1-y}I_3$, and c) $Cs_{0.15}FA_{0.85}Sn_zPb_{1-z}I_3$. The FWHM from main perovskite peak respect to the Sn fraction of d) $MASn_xPb_{1-x}I_3$, e) $FASn_yPb_{1-y}I_3$, and f) $Cs_{0.15}FA_{0.85}Sn_zPb_{1-z}I_3$.

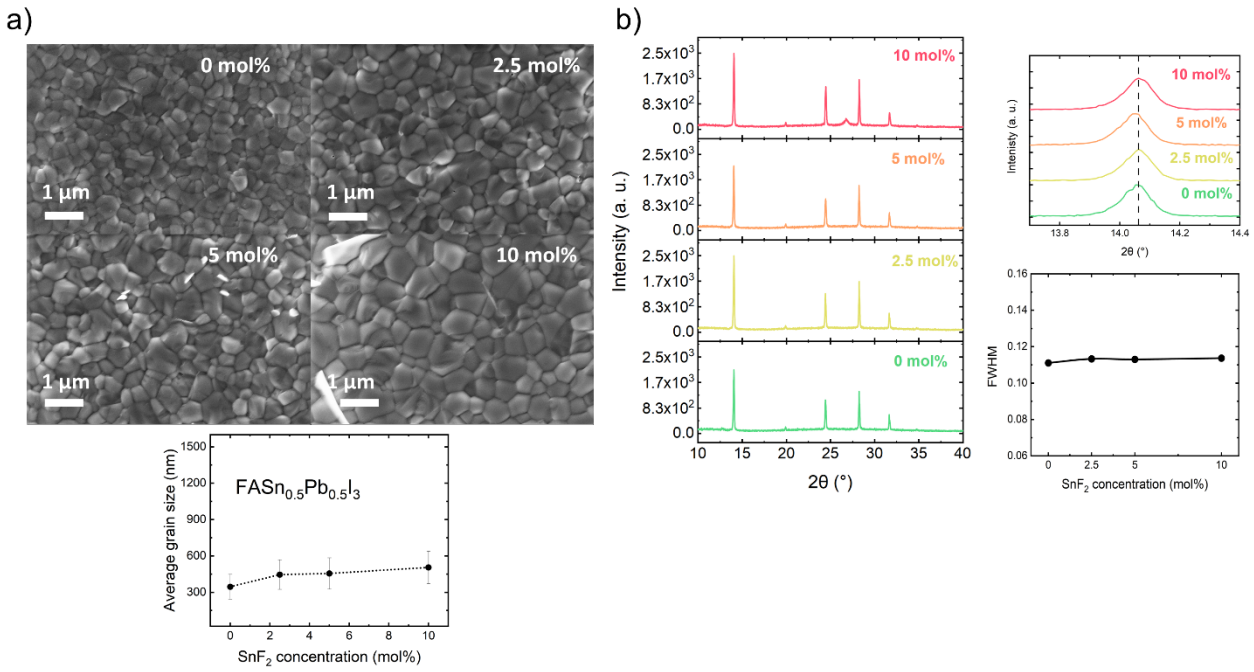

Fig. S11 a) SEM images from the $FASn_{0.5}Pb_{0.5}I_3$ samples with different concentrations of SnF_2; the average grain size as a function of the SnF_2 concentration is also presented. b) XRD patterns from the $FASn_{0.5}Pb_{0.5}I_3$ samples with different concentrations of SnF_2. The characteristic perovskite peak and FWHM do not vary significantly with the addition of SnF_2.

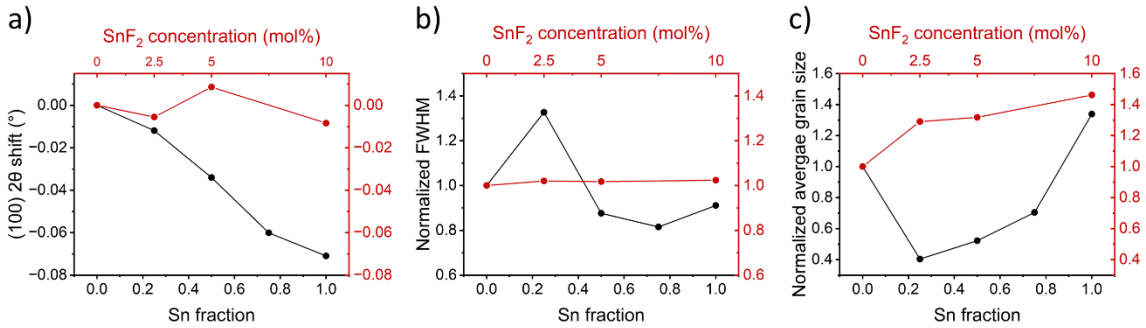

Fig. S12. Differences between varying SnF_2 concentration and Sn-content on the a) (100) 2θ shift, b) normalized FWHM, and c) normalized average grain size. The composition of the A-cation where Sn fraction is varied is FA. The composition for the samples where SnF_2 content is modified is $FASn_{0.5}Pb_{0.5}I_3$. When comparing differences in FWHM and 2θ shift from the (100) reflection between samples where we changed Sn fraction and SnF_2 concentration, we observed that SnF_2 concentration has minimal effect on these variables compared to Sn fraction. In terms of grain size, we noticed that varying Sn content can lead to grain size changes of up to 300%. In contrast, SnF_2 only enlarges the grain up to 40%. While we acknowledge that the effect of SnF_2 on grain size influence ion migration pathways, we have noticed that morphology changes alone cannot explain the large variations recorded in conductivity. In our previous research, we have observed that regardless of the significant morphology differences across multiple Sn-based perovskites, we have found that A-site composition and Sn content correlate stronger with the most significant changes in conductivity.[32, 33] Additionally, the conductivity reported herein are within the values range of films with similar composition ($MAPb_{0.5}Sn_{0.5}I_3$) but completely different morphology.[34] Therefore,

we consider that besides morphology, other key aspects discussed in this work are necessary to have a complete understanding on the ionic-electronic transport properties of these materials.

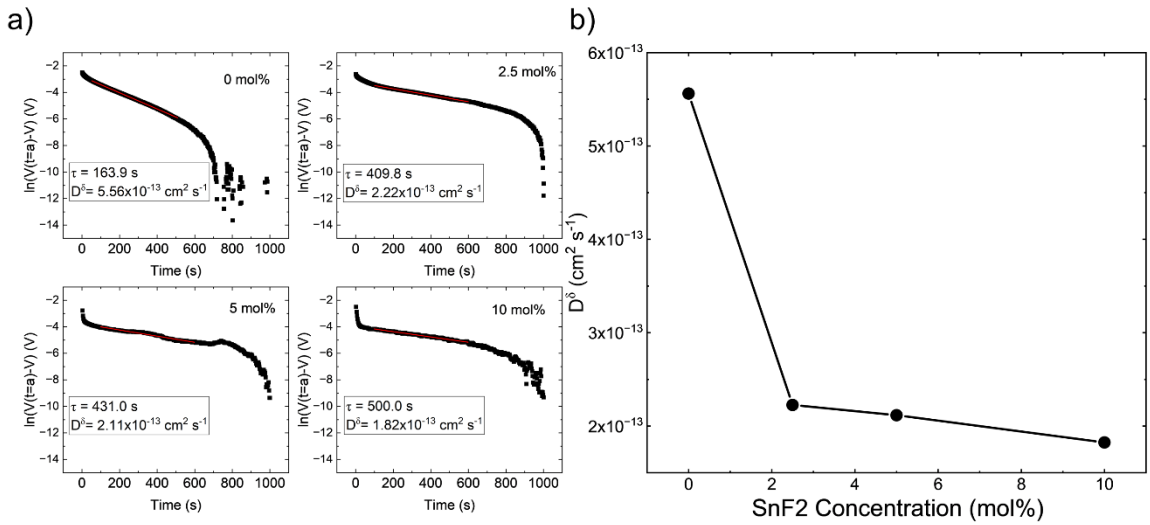

Fig. S13 a) Semi-log plots of voltage versus time. b) Chemical diffusion coefficient (D^{δ}) as a function of SnF_2 concentration of the $FASn_{0.5}Pb_{0.5}I_3$ samples. While the relatively constant μ_h with the addition of SnF_2 suggests that the reduction in the D^{δ} might be indicative of a lower D_{ion} and consequently a lower μ_{ion}, the complex interplay between the electronic and ionic components makes it challenging to quantify the individual contribution of μ_{ion} to D^{δ}.

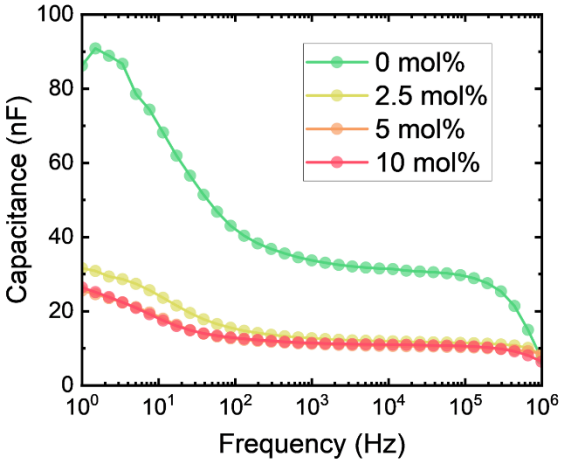

Fig. S14 Capacitance as a function of frequency from $FASn_{0.5}Pb_{0.5}I_3$ (0, 2.5, 5, and 10 mol% SnF_2) samples. The ε was inferred from the capacitance at 10 kHz of the 10 mol% samples. We note that 0 mol% sample capacitance differs significantly from the rest of the samples. As shown by others, this difference can be explained due to the high ionic density, which could lead to a miscalculation of ε.[19] Magnetospectroscopy measurements have revealed that ε do not differ significantly between compositions with high Sn content (>0.6) and low Sn content (0.2), in samples without SnF_2.[35]

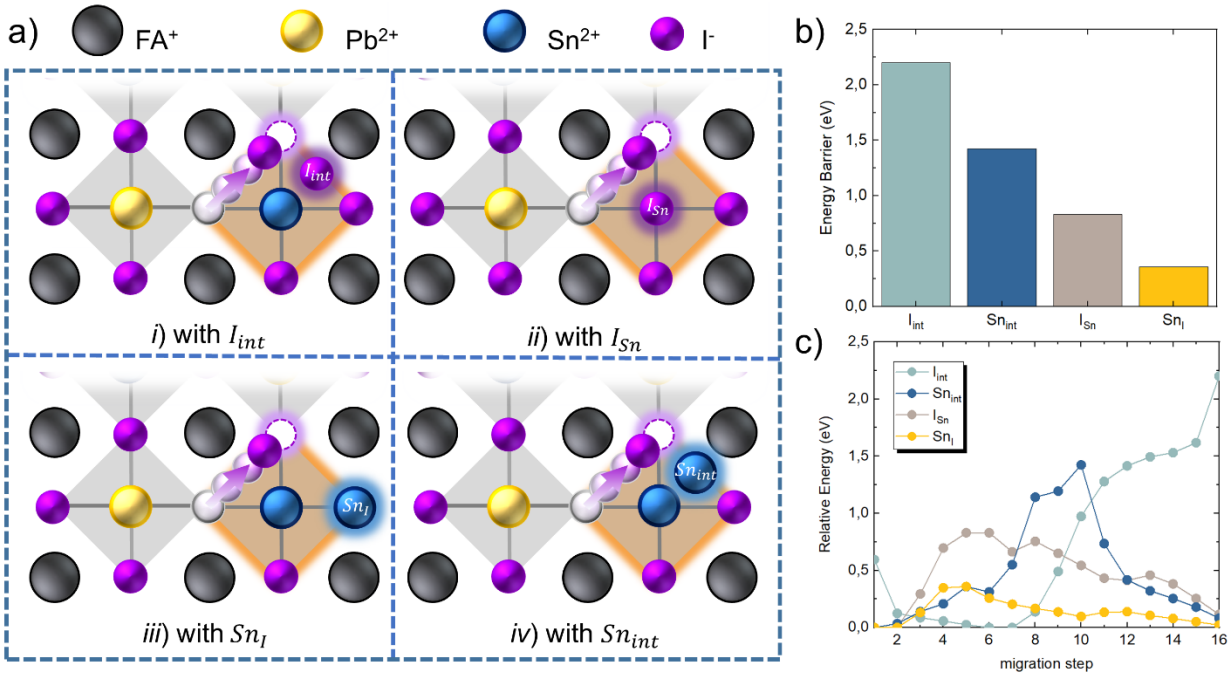

Fig. S15 a) Theoretical model of the iodide migration pathway in a $FAPb_{0.5}Sn_{0.5}I_3$ lattice under four scenarios: i) I_{int}, ii) I_{Sn} , iii) Sn_I, and iv) Sn_{int}. b) The energy barriers for iodide migration of each proposed scenario and c) relative energy landscapes of the system during iodide migration.

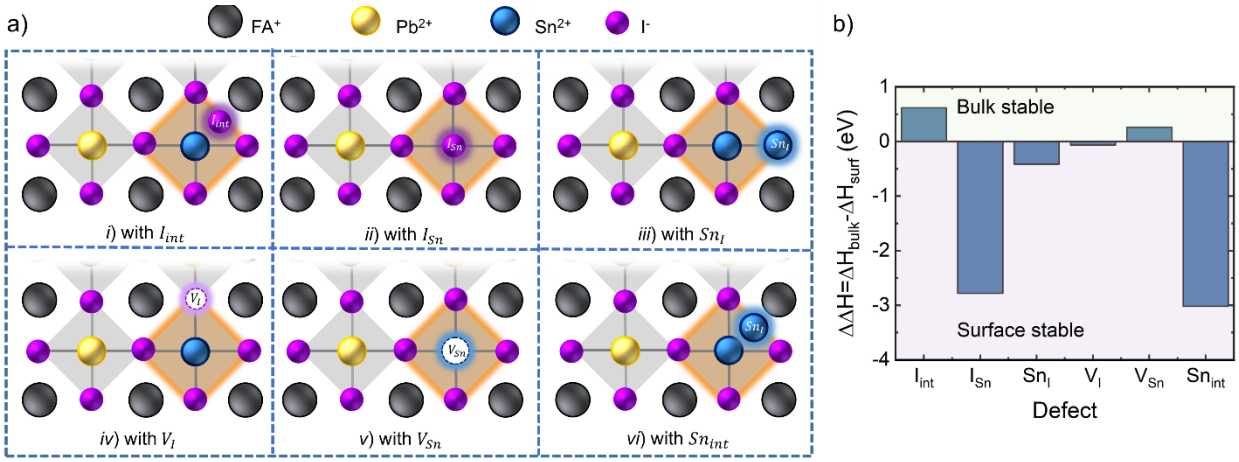

Fig. S16 a) theoretical model of the defect formation energy on a $FAPb_{0.5}Sn_{0.5}I_3$ lattice, the six defects considered are: i) I_{int}, ii) I_{Sn} , iii) Sn_I, iv) V_I, v) V_{Sn}, vi) Sn_{int}. b) Formation energy difference ($\Delta\Delta H = \Delta H_{bulk} - \Delta H_{surf}$) as a function each defect.

a)

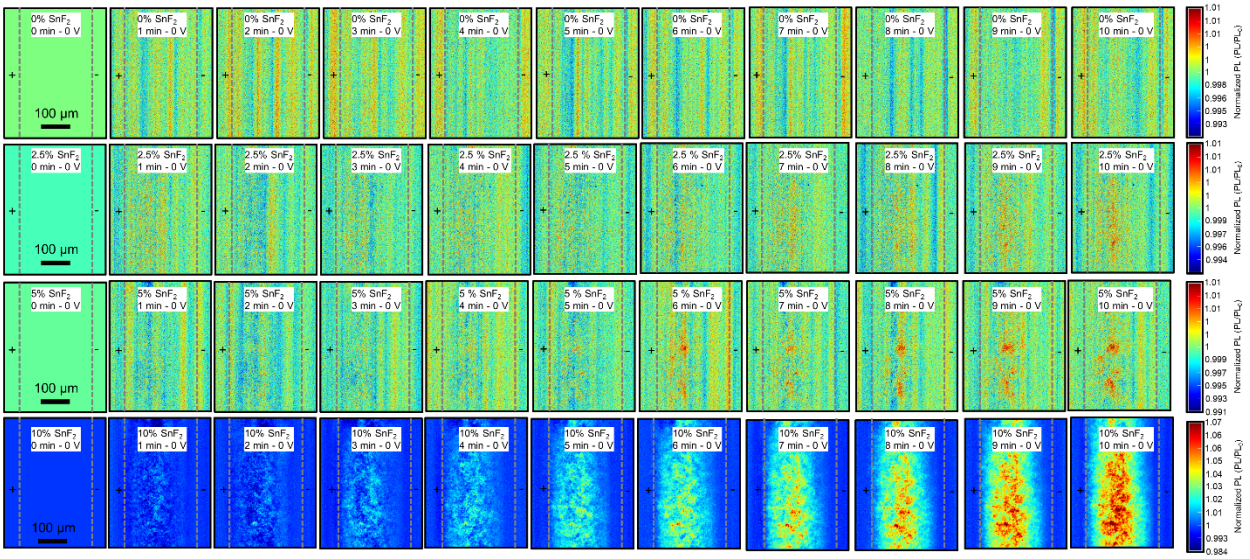

b)

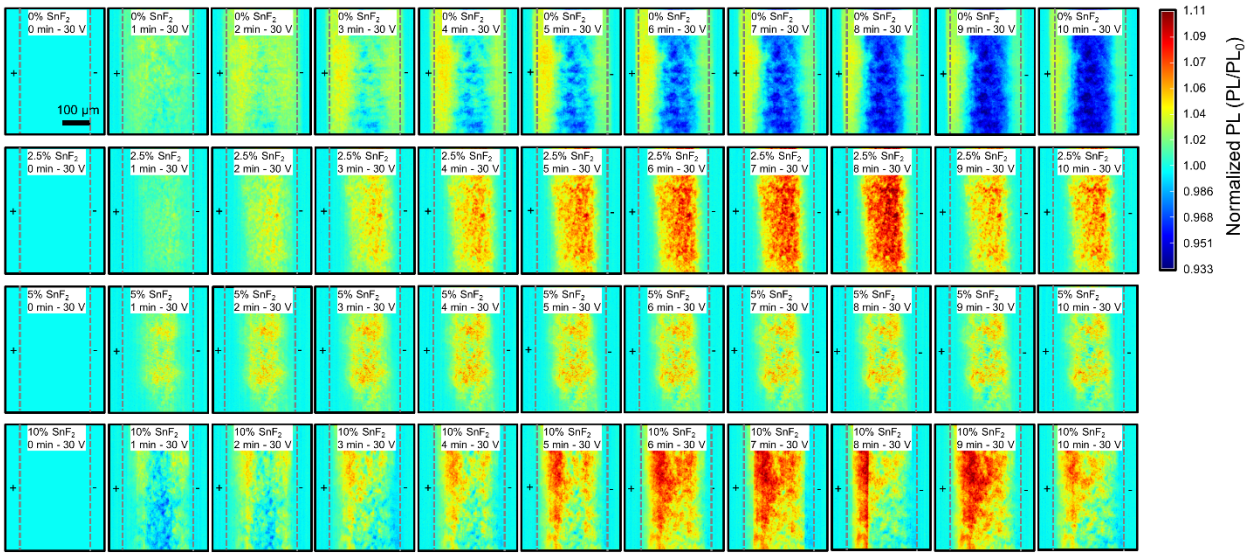

Fig. S17 Hyperspectral PL mapping performed on lateral samples (channel length is 300 µm) of $FASn_{0.5}Pb_{0.5}I_3$ (0, 2.5, 5, and 10 mol% SnF_2) upon a) 0V and b) 30 V bias. For 0 V images, each composition is represented with its own color bar scale, while 30 V images are represented with a common color bar scale. PL images are normalized vs the image at t = 0 min for each composition. Straight, vertical lines in some images correspond to measurement noise due to unchanging PL intensity versus the t = 0 min image.

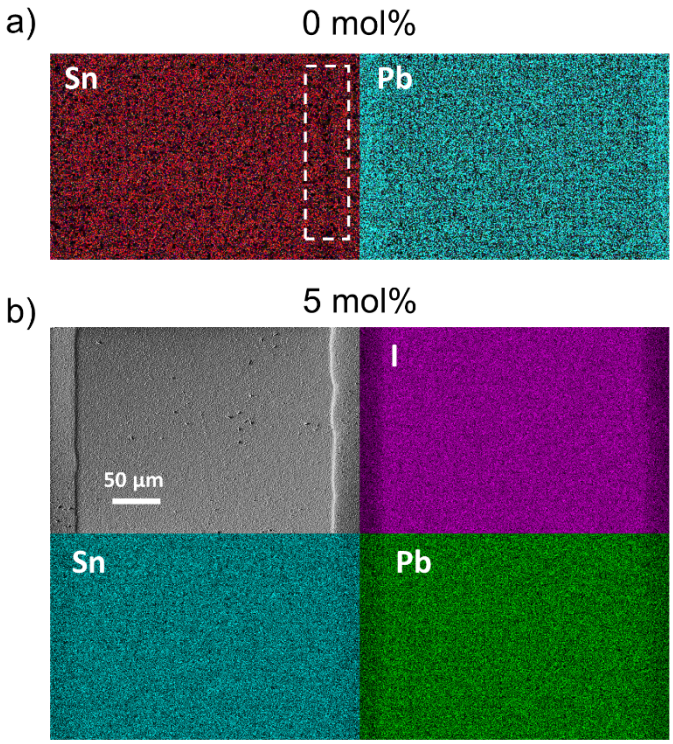

Fig. S18 SEM-EDS elemental mapping showing the distribution of a) Sn and Pb for the 0 mol% sample and b) I, Sn, and Pb for the 5 mol% sample after being biased at 30 V for 1 hr.

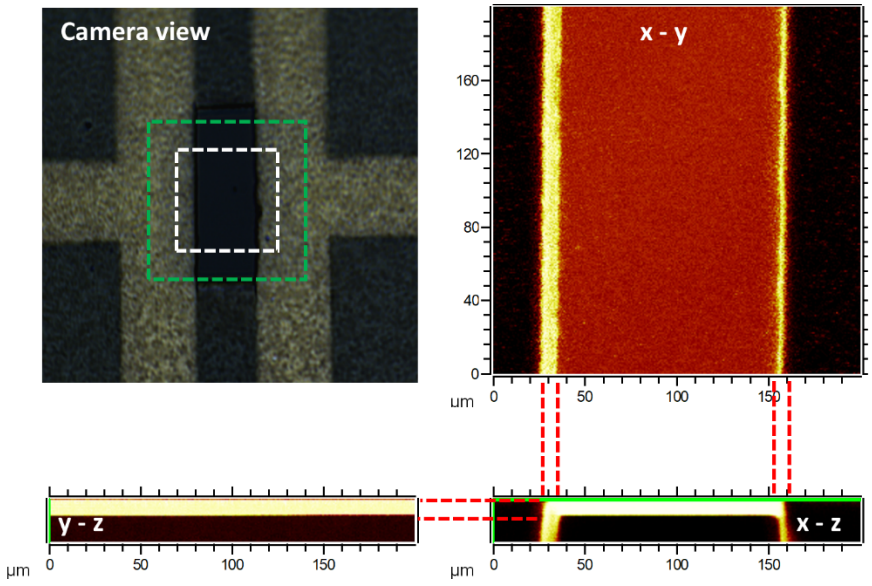

Fig. S19 Schematic of a complete x - y, x - z and y - z series of ion images from one of the analysed samples.

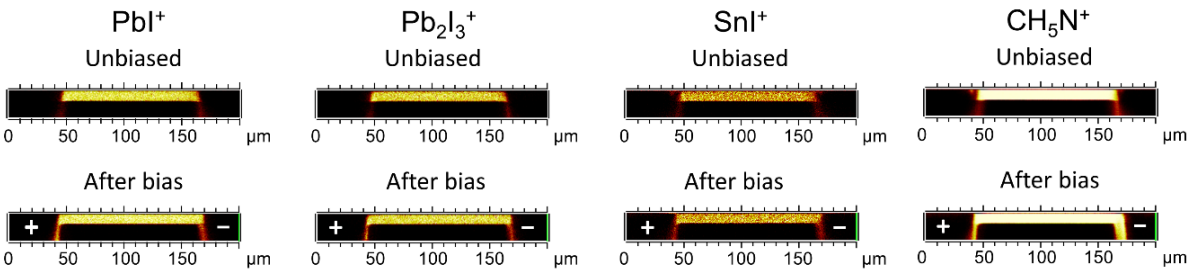

Fig. S20 ToF-SIMS depth profiles of the different chemical species (PbI^+, $Pb_2I_3^+$, SnI^+, and CH_5N^+) from the 0 mol% SnF_2 samples before and after bias. The samples were stressed at 27 V for 1 hour. The channel length of the sample is 150 um, we used the same lateral configuration as the samples prepared for galvanostatic polarization measurement.

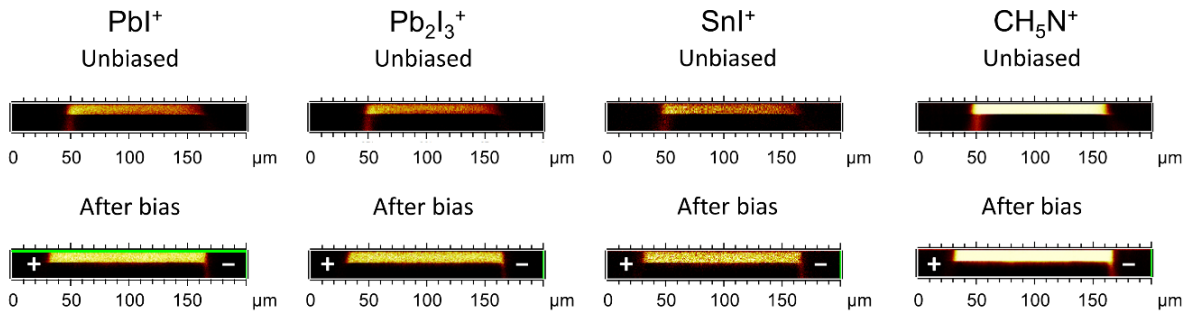

Fig. S21 ToF-SIMS depth profiles of the different chemical species (PbI^+, $Pb_2I_3^+$, SnI^+, and CH_5N^+) from the 5 mol% SnF_2 samples before and after bias. The samples were stressed under the same conditions as 0 mol% SnF_2 samples.

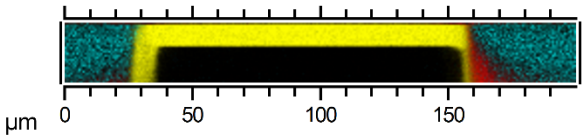

Fig. S22 Depth profile image showcasing the channel (represented by the perovskite constituent ion indicated by the yellow color) and the Au_3^+ and Cr^+ secondary ions (showed in blue and red color, respectively) for an example system.

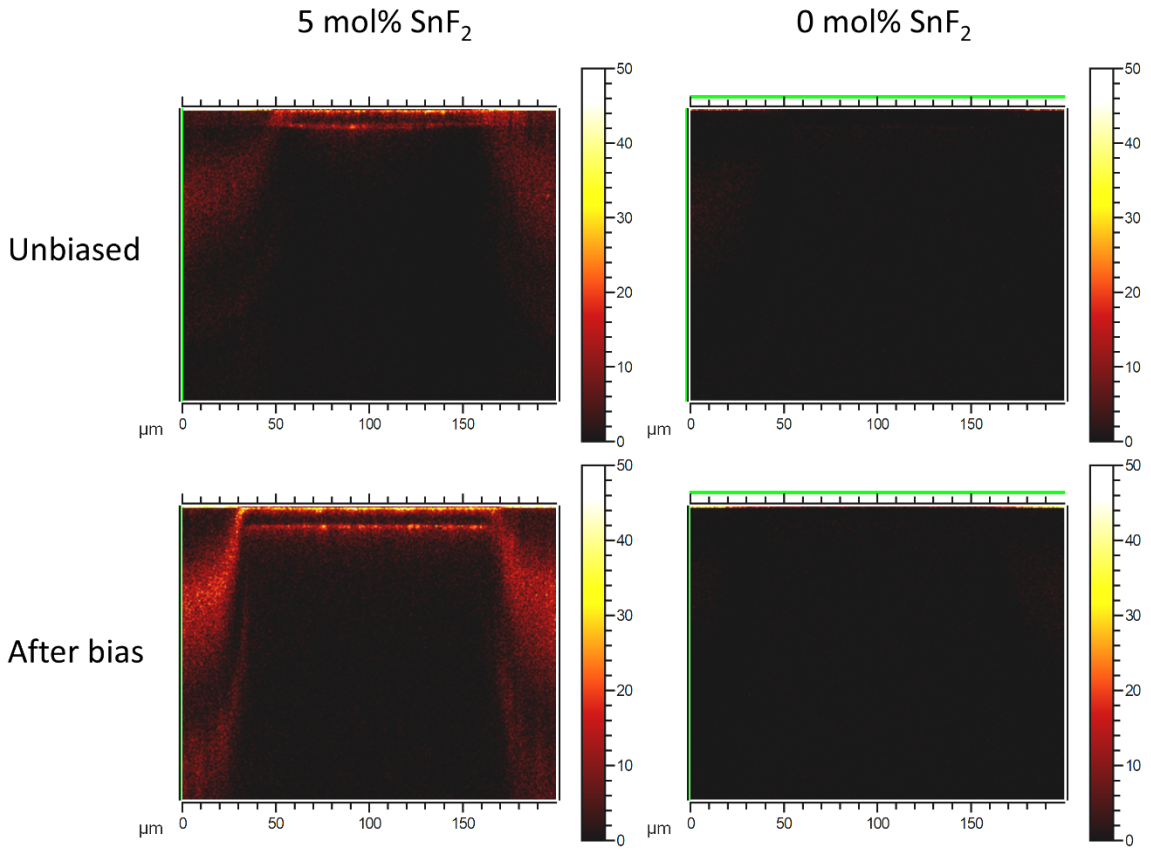

Fig. S23 ToF-SIMS depth profile maps of F^- ions before and after biasing at 30 V from the 0 and 5 mol% SnF_2 samples. We observe that the excess of tin fluorides (SnF_4 or SnF_2) accumulates at the bottom and top interfaces but no preferential accumulation of F^- ions occur after biasing the sample. Considering these results, the relatively small number of F^- ions compared to I^-, the strong electronegativity of F^- ions, the relative stability of the stannous fluorides compared to stannous iodides (SnI_2 or SnI_4), and the symmetric PL response during biasing, we find unlikely that F^- migration is a dominant process. Furthermore, we acknowledge the possibility of F- ions passivating defects located at the bottom-top surfaces and grain boundaries. Since defect passivation has a significant influence on ion migration,[36] it is plausible that passivation from SnF_2 have a role in decreasing σ_{ion} and n_{ion}. However, based on our simulation we also observe that V_{Sn}^{2-} and h^+ (both variables being heavily influenced by SnF_2) [15, 37, 38] are critical to reduce the energy barriers for I^- migration. While we do not discard a competing mechanism, herein we highlight the importance of point defects and carriers on the ion transport in Sn-based perovskites.

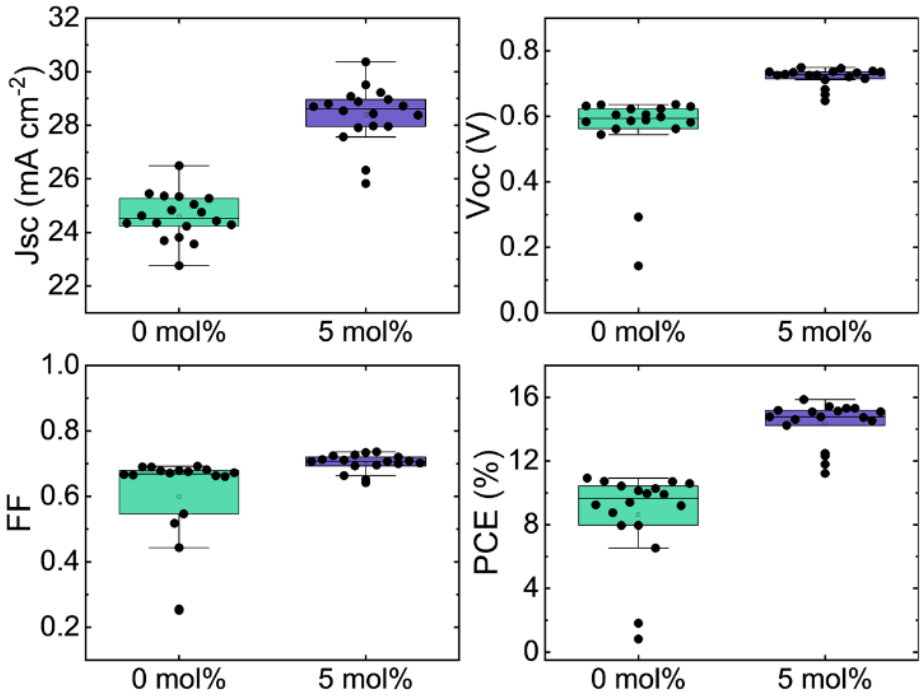

Fig. S24 Box plots of the photovoltaic parameters relative to the SnF_2 concentration (0 and 5 mol%), device architecture is ITO/PEDOT:PSS/$Cs_{0.25}FA_{0.75}Sn_{0.5}Pb_{0.5}I_3$/$C_{60}$/BCP/Cu.

Supplementary references

1. G. Y. Kim, A. Senocrate, T.-Y. Yang, G. Gregori, M. Grätzel and J. Maier, *Nat. Mater.*, 2018, **17**, 445-449.
2. G. Y. Kim, A. Senocrate, Y.-R. Wang, D. Moia and J. Maier, *Angewandte Chemie International Edition*, 2021, **60**, 820-826.
3. A. Senocrate, I. Spanopoulos, N. Zibouche, J. Maier, M. S. Islam and M. G. Kanatzidis, *Chem. Mater.*, 2021, **33**, 719-726.
4. Y. Zhang, A. Ummadisingu, R. Shivanna, D. H. L. Tjhe, H.-I. Un, M. Xiao, R. H. Friend, S. P. Senanayak and H. Sirringhaus, *Small*, 2023, **19**, 2302494.
5. A. Guerrero, J. You, C. Aranda, Y. S. Kang, G. Garcia-Belmonte, H. Zhou, J. Bisquert and Y. Yang, *ACS Nano*, 2016, **10**, 218-224.
6. M. García-Batlle, O. Baussens, S. Amari, J. Zaccaro, E. Gros-Daillon, J.-M. Verilhac, A. Guerrero and G. Garcia-Belmonte, *Adv. Electron. Mater.*, 2020, **6**, 2000485.
7. R. A. Kerner, L. Zhao, S. P. Harvey, J. J. Berry, J. Schwartz and B. P. Rand, *ACS Energy Lett.*, 2020, **5**, 3352-3356.
8. R. A. Kerner, A. V. Cohen, Z. Xu, A. R. Kirmani, S. Y. Park, S. P. Harvey, J. P. Murphy, R. C. Cawthorn, N. C. Giebink, J. M. Luther, K. Zhu, J. J. Berry, L. Kronik and B. P. Rand, *Adv. Mater.*, 2023, **35**, 2302206.
9. W. Ming, D. Yang, T. Li, L. Zhang and M.-H. Du, *Advanced Science*, 2018, **5**, 1700662.
10. J. C. Pérez-Martínez, M. Berruet, C. Gonzales, S. Salehpour, A. Bahari, B. Arredondo and A. Guerrero, *Adv. Funct. Mater.*, 2023, **33**, 2305211.
11. Z. Xu, R. A. Kerner, S. P. Harvey, K. Zhu, J. J. Berry and B. P. Rand, *ACS Energy Lett.*, 2023, **8**, 513-520.
12. G. F. Samu, Á. Balog, F. De Angelis, D. Meggiolaro, P. V. Kamat and C. Janáky, *J. Am. Chem. Soc.*, 2019, **141**, 10812-10820.

13. S. Martani, Y. Zhou, I. Poli, E. Aktas, D. Meggiolaro, J. Jiménez-López, E. L. Wong, L. Gregori, M. Prato, D. Di Girolamo, A. Abate, F. De Angelis and A. Petrozza, *ACS Energy Lett.*, 2023, **8**, 2801-2808.
14. K. J. Savill, A. M. Ulatowski and L. M. Herz, *ACS Energy Lett.*, 2021, **6**, 2413-2426.
15. J. Pascual, M. Flatken, R. Félix, G. Li, S.-H. Turren-Cruz, M. H. Aldamasy, C. Hartmann, M. Li, D. Di Girolamo, G. Nasti, E. Hüsam, R. G. Wilks, A. Dallmann, M. Bär, A. Hoell and A. Abate, *Angewandte Chemie International Edition*, 2021, **60**, 21583-21591.
16. D. Meggiolaro, D. Ricciarelli, A. A. Alasmari, F. A. S. Alasmary and F. De Angelis, *J. Phys. Chem. Lett.*, 2020, **11**, 3546-3556.
17. K. P. Marshall, M. Walker, R. I. Walton and R. A. Hatton, *Nat. Energy*, 2016, **1**, 16178.
18. A. Senocrate, I. Moudrakovski, G. Y. Kim, T.-Y. Yang, G. Gregori, M. Grätzel and J. Maier, *Angewandte Chemie International Edition*, 2017, **56**, 7755-7759.
19. J. Diekmann, F. Peña-Camargo, N. Tokmoldin, J. Thiesbrummel, J. Warby, E. Gutierrez-Partida, S. Shah, D. Neher and M. Stolterfoht, *J. Phys. Chem. Lett.*, 2023, **14**, 4200-4210.
20. D. Moia, I. Gelmetti, P. Calado, W. Fisher, M. Stringer, O. Game, Y. Hu, P. Docampo, D. Lidzey, E. Palomares, J. Nelson and P. R. F. Barnes, *Energy Environ. Sci.*, 2019, **12**, 1296-1308.
21. M. C. Schmidt, A. O. Alvarez, J. J. de Boer, L. J. M. van de Ven and B. Ehrler, *ACS Energy Lett.*, 2024, **9**, 5850-5858.
22. A. Schiller, S. Jenatsch, B. Blülle, M. A. Torre Cachafeiro, F. Ebadi, N. Kabir, M. Othman, C. M. Wolff, A. Hessler-Wyser, C. Ballif, W. Tress and B. Ruhstaller, *J. Phys. Chem. Lett.*, 2024, **15**, 11252-11258.
23. C. Zhao, B. Chen, X. Qiao, L. Luan, K. Lu and B. Hu, *Adv. Energy Mater.*, 2015, **5**, 1500279.
24. K. J. Savill, A. M. Ulatowski, M. D. Farrar, M. B. Johnston, H. J. Snaith and L. M. Herz, *Adv. Funct. Mater.*, 2020, **30**, 2005594.
25. L. Huerta Hernandez, L. Lanzetta, S. Jang, J. Troughton, M. A. Haque and D. Baran, *ACS Energy Lett.*, 2022, **8**, 259-273.
26. L. Lanzetta, T. Webb, N. Zibouche, X. Liang, D. Ding, G. Min, R. J. E. Westbrook, B. Gaggio, T. J. Macdonald, M. S. Islam and S. A. Haque, *Nat. Commun.*, 2021, **12**, 2853.
27. L. Lanzetta, T. Webb, J. M. Marin-Beloqui, T. J. Macdonald and S. A. Haque, *Angewandte Chemie International Edition*, 2023, **62**, e202213966.
28. A. Alsulami, L. Lanzetta, L. Huerta Hernandez, D. Rosas Villalva, A. Sharma, S. P. Gonzalez Lopez, A.-H. Emwas, A. Yazmaciyan, F. Laquai, I. Yavuz and D. Baran, *J. Am. Chem. Soc.*, 2024, **146**, 22970-22981.
29. D. Di Girolamo, N. Phung, F. U. Kosasih, F. Di Giacomo, F. Matteocci, J. A. Smith, M. A. Flatken, H. Köbler, S. H. Turren Cruz, A. Mattoni, L. Cinà, B. Rech, A. Latini, G. Divitini, C. Ducati, A. Di Carlo, D. Dini and A. Abate, *Adv. Energy Mater.*, 2020, **10**, 2000310.
30. S. Sandrez, Z. Molenda, C. Guyot, O. Renault, J.-P. Barnes, L. Hirsch, T. Maindron and G. Wantz, *Adv. Electron. Mater.*, 2021, **7**, 2100394.
31. M. Kim, G.-H. Kim, T. K. Lee, I. W. Choi, H. W. Choi, Y. Jo, Y. J. Yoon, J. W. Kim, J. Lee, D. Huh, H. Lee, S. K. Kwak, J. Y. Kim and D. S. Kim, *Joule*, 2019, **3**, 2179-2192.
32. M. A. Haque, L. H. Hernandez, B. Davaasuren, D. R. Villalva, J. Troughton and D. Baran, *Advanced Energy and Sustainability Research*, 2020, **1**, 2000033.
33. R. Tounesi, L. H. Hernandez, L. Lanzetta, S. Jang, B. Davaasuren, M. A. Haque and D. Baran, *ACS Applied Electronic Materials*, 2023, **6**, 2826-2831.
34. J. Euvrard, O. Gunawan, X. Zhong, S. P. Harvey, A. Kahn and D. B. Mitzi, *Materials Advances*, 2021, **2**, 2956-2965.
35. K. Galkowski, A. Surrente, M. Baranowski, B. Zhao, Z. Yang, A. Sadhanala, S. Mackowski, S. D. Stranks and P. Plochocka, *ACS Energy Lett.*, 2019, **4**, 615-621.
36. J. Xing, Q. Wang, Q. Dong, Y. Yuan, Y. Fang and J. Huang, *Physical Chemistry Chemical Physics*, 2016, **18**, 30484-30490.
37. J. Zillner, H.-G. Boyen, P. Schulz, J. Hanisch, N. Gauquelin, J. Verbeeck, J. Küffner, D. Desta, L. Eisele, E. Ahlswede and M. Powalla, *Adv. Funct. Mater.*, 2022, **32**, 2109649.
38. Q. Chen, J. Luo, R. He, H. Lai, S. Ren, Y. Jiang, Z. Wan, W. Wang, X. Hao, Y. Wang, J. Zhang, I. Constantinou, C. Wang, L. Wu, F. Fu and D. Zhao, *Adv. Energy Mater.*, 2021, **11**, 2101045.